SUPPLEMENTARY NOTE 1: X-RAY PHOTOELECTRON SPECTRA FROM AS-GROWN VSe_2 ON $NbSe_2$

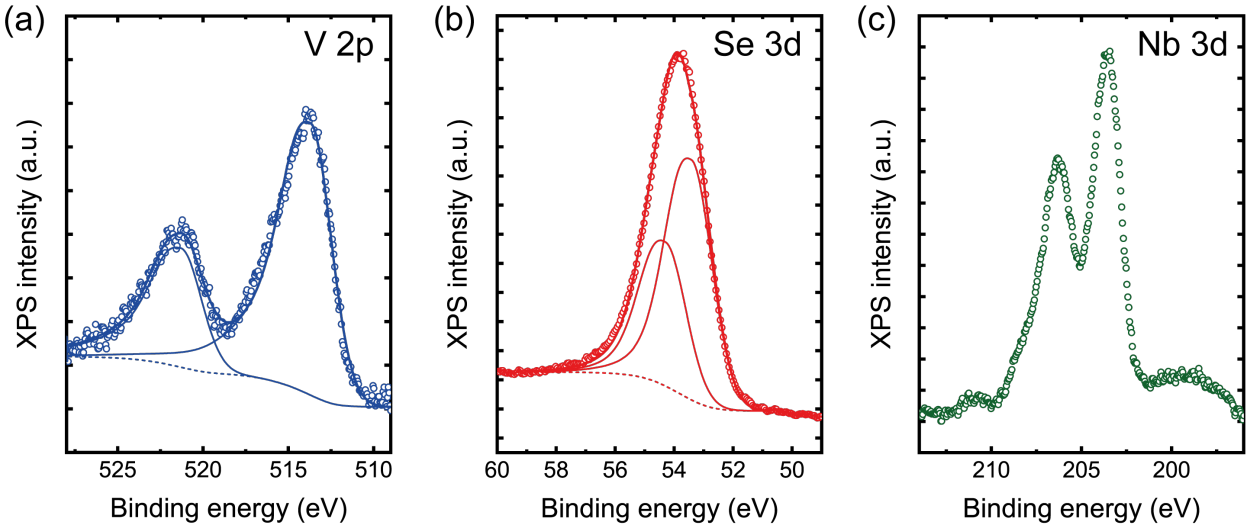

Supplementary Figure 1. X-ray photoelectron spectra (XPS) from a 0.6 monolayer (ML) as-grown VSe_2 film on $NbSe_2$. (a) V 2p region. (b) Se 3d region fitted with two Gaussian/Lorentzian peaks corresponding to the $3d_{5/2}$ and $3d_{3/2}$ peaks. (c) Nb 3d region.

SUPPLEMENTARY NOTE 2: COMPUTATIONAL DETAILS

All density-functional theory calculations are carried out in the plane-wave basis in the projector augmented wave framework as implemented in VASP [1–3]. In all calculations, we use 500 eV cutoff and k-point sampling corresponding to 24×24 mesh in the primitive cell. High k-point mesh is required to correctly describe e.g. the CDW phases.

V tends to exhibit strong Coulomb correlations, which usually necessitates using either hybrid functionals or $+U$. It was shown in Ref. [4], the depending on the U-parameter, the monolayer is either in nonmagnetic CDW state or in ferromagnetic no-CDW state. This balance is also affected by the number of electrons [4] and likely also by strain.

We calculated the lattice constants and magnetic moments using several exchange-correlation functionals [5–7] in order to choose a suitable one. The results are shown in Supplementary Table 1 and also in Supplementary Figure 2. In the case of H-$NbSe_2$, all three tested functionals appear to give reasonable description of the lattice constant. In the case

of T-VSe_2, we first note, that the bulk lattice constant (3.355 Å) is smaller than the one measured here for monolayer from STM images (about 3.5 ± 0.1 Å), which could be due to the transition between FM/CDW phases.

LDA strongly underestimates all lattice constants, but PBE, PBE-D2, and revB86b all slightly underestimates the lattice constant, although usually expected to overestimate. In all cases, adding Hubbard-like on-site Coulomb interaction remedies the situation. At moderate values of the U-parameter (1-2 eV), the lattice constants are close to the HSE value and between the two experimental values, and also the magnetic moments are close to the HSE value. At large U, both the lattice constant and the magnetic moment increase.

We also studied the CDW phase stability. We here only considered the $\sqrt{3}$R30$\times\sqrt{7}$R19.1 pattern suggested in Ref. [8]. As shown in the calculated phonon dispersion curves in Sup-

Supplementary Table 1. The calculated lattice constants and magnetic moments of monolayer $NbSe_2$ and VSe_2. The experimental lattice constants are also shown and taken from the bulk. ΔE_{CDW} is the energy difference between $\sqrt{3}$R30$\times\sqrt{7}$R19.1 charge-density wave (CDW) phase and ferromagnetic (FM) phase (positive value means FM phase is lower in energy).

	H-$NbSe_2$		T-VSe_2		
	a (Å)	M (μ_{B})	a (Å)	M (μ_{B})	ΔE_{CDW} (eV)
Expt. a	3.442		3.355		
PBE	3.486	-	3.336	0.6	0.013
PBE ($U = 1$)			3.405	1.1	
PBE ($U = 2$)			3.406	1.2	
PBE-D2	3.467	-	3.321	0.6	
revB86b	3.461	-	3.306	0.5	0.004
revB86b ($U = 1$)			3.356	0.9	
revB86b ($U = 2$)			3.408	1.2	0.161
revB86b ($U = 3$)			3.451	1.3	
revB86b ($U = 4$)			3.468	1.5	
revB86b ($U = 5$)			3.488	1.6	
LDA			3.220	0.2	-0.007
HSE			3.396	1.0	

Supplementary Table 2. The calculated lattice constants and magnetic moments of unstrained monolayer H-VSe_2. $\Delta E_{H/T}$ is the energy difference between the H- and T-phases at the optimized lattice constant (positive value means 1T phase is lower in energy).

	H-VSe_2		
	a (Å)	M (μ_B)	$\Delta E_{H/T}$
PBE	3.335	1.0	-0.045
revB86b	3.295	1.0	-0.017
revB86b ($U = 2$)	3.339	1.0	0.001
revB86b ($U = 5$)	3.454	1.1	0.623
HSE	3.312	1.0	-0.033

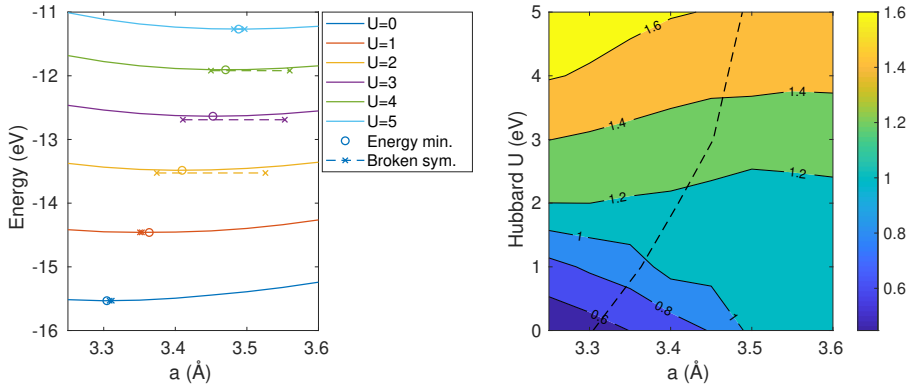

Supplementary Figure 2. (a) Total energy vs. lattice constant for different values of U-parameter calculated using revB86b. The energy minimum position is highlighted with a circle. The lattice constants and energy of the broken symmetry configuration are shown with crosses. (b) Map of magnetic moments in the U/a space. Dashed line denotes the optimal lattice constants.

plementary Figure 3, the imaginary frequency modes are located at the same wavevectors, which justifies using the same CDW pattern with all functionals. The energy difference between this phase and the FM phase are also given in Supplementary Table 1. Only within LDA, CDW phase is slightly lower in energy (by 7 meV/formula unit), whereas PBE and revB86b both slightly favor FM phase (by 4–13 meV/f.u.). Upon adding $+U$ correction the FM phase becomes strongly favored.

We note, that for U values in the range 2–4 eV, a lower energy FM structure with broken

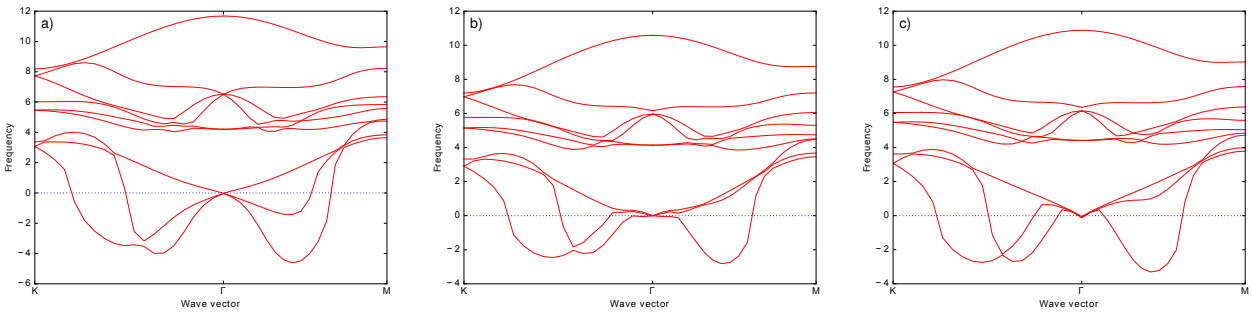

Supplementary Figure 3. Phonon dispersion spectra in the nonmagnetic (NM) phase calculated using (a) LDA, (b) PBE, and (c) revB86b.

symmetry was found (cf. Supplementary Figure 2). The unit cell size remains at 3 atoms, but the two lattice constants have different lengths.

As a result, revB86b with moderate U (e.g. 2 eV) gives results in good agreement with HSE and also lattice constant in fairly good agreement with experiments. On the other hand, the CDW phase can be stabilized, or nearly stabilized, only without U.

The corresponding results for H-phase VSe_2 are given in Supplementary Table 2. With no $+U$ correction, H-phase is slightly lower in energy than the T-phase. The energies are equal at $U = 2$ eV and with higher values of U T-phase is strongly favored. HSE results are again closer to the results with higher values of U. The lattice constants are generally slightly smaller than for T-phase. The magnetic moments are close to 1 μ_B in all cases.

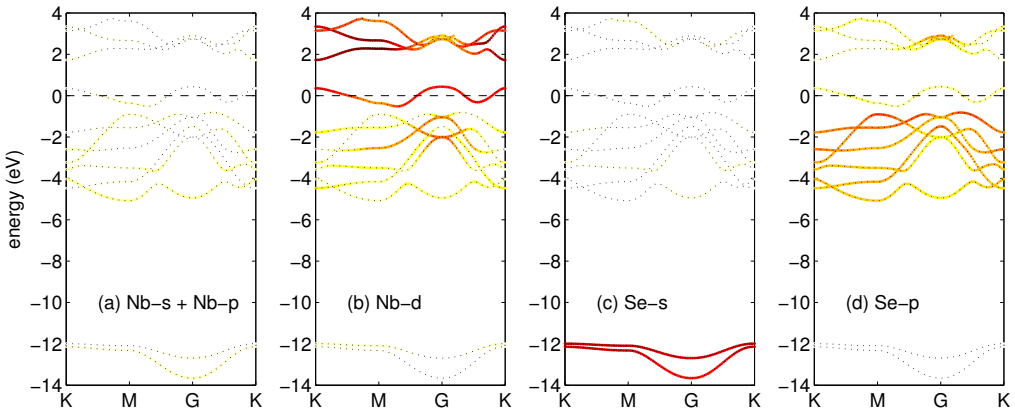

Supplementary Figure 4. Band structure of monolayer H-$NbSe_2$ projected on (a) Nb-sp, (b) Nb-d, (c) Se-s, and (d) Se-p. Energy zero is at Fermi-level.

Electronic structure: Band structure of monolayer $NbSe_2$ is shown in Supplementary Figure 4. The valence bands are all formed out of Nb-d and Se-p. Fermi-level crosses one distinct band, which is also responsible for the CDW. Spin-orbit coupling splits this band by 0.19–0.31 eV.

Band structure of monolayer T-VSe_2 is shown in Supplementary Figure 5. There is partly filled V-d band, similar to $NbSe_2$. $+U$ parameter controls the separation between the spin-up and -down channels of this band. Band structure of monolayer H-VSe_2 is shown in Supplementary Figure 6. The semiconducting vs metallic character is sensitive to the U-parameter. Without $+U$ the system is barely semiconducting with a gap of about 90 meV. There is a sizeable gap at $U = 2$ eV, but the gap has closes again at $U = 5$ eV.

The PBE calculated work functions are 5.56 eV for $NbSe_2$ and 5.02 eV for VSe_2. Thus, we expect to have electron transfer from VSe_2 to $NbSe_2$ (hole-doping of VSe_2). Comparing these to the Fermi-level position of graphene at 4.39 eV suggests charge transfer from graphene to VSe_2 (electron-doping of VSe_2). According to Fumega and Pardo [4], FM becomes stronger at small hole-doping and weaker at electron-doping (assuming Stoner mechanism).

CDW structures: Bulk $NbSe_2$ adopts incommensurate CDW phase, although nearly commensurate to 3×3 [9], at $T < 33$ K. Calculations are carried out at 0 K and thus also show CDW-phase when suitable supercell is used. In 3×3 monolayer supercell, PBE and revB86b calculations yield CDW-phase lower in energy by 4 meV (33 K·k_B) per formula unit.

There are two nearly degenerate phases for the CDW distortion, hexagon-centered (HC) and anion-centered (AC) [10]. These are shown in Supplementary Figure 7.

Atomic structure of the CDW phase VSe_2 is shown in Supplementary Figure 8.

CDW structures: In bulk H-$NbSe_2$, Nb atoms are on top of each other and Se atoms positions alternate. Bulk T-VSe_2 adopts an AA stacking.

The experimentally measured lattice constants are very similar, and thus it should be safe to use just a unit cell when studying the stacking in the $NbSe_2$/VSe_2 heterostructure.

Fixing H-$NbSe_2$ to BaB, T-VSe_2 can be located at BaC, CbA, and AcB, or inverted at CaB, AbC, and BcA. The binding energies are listed in Supplementary Table 3, and defined with respect to strained monolayers, so that it only contains the interlayer binding contribution. The results without $+U$ show large changes in the magnetic moment, indicating sensitivity of the system to converge to either FM or NM phase.

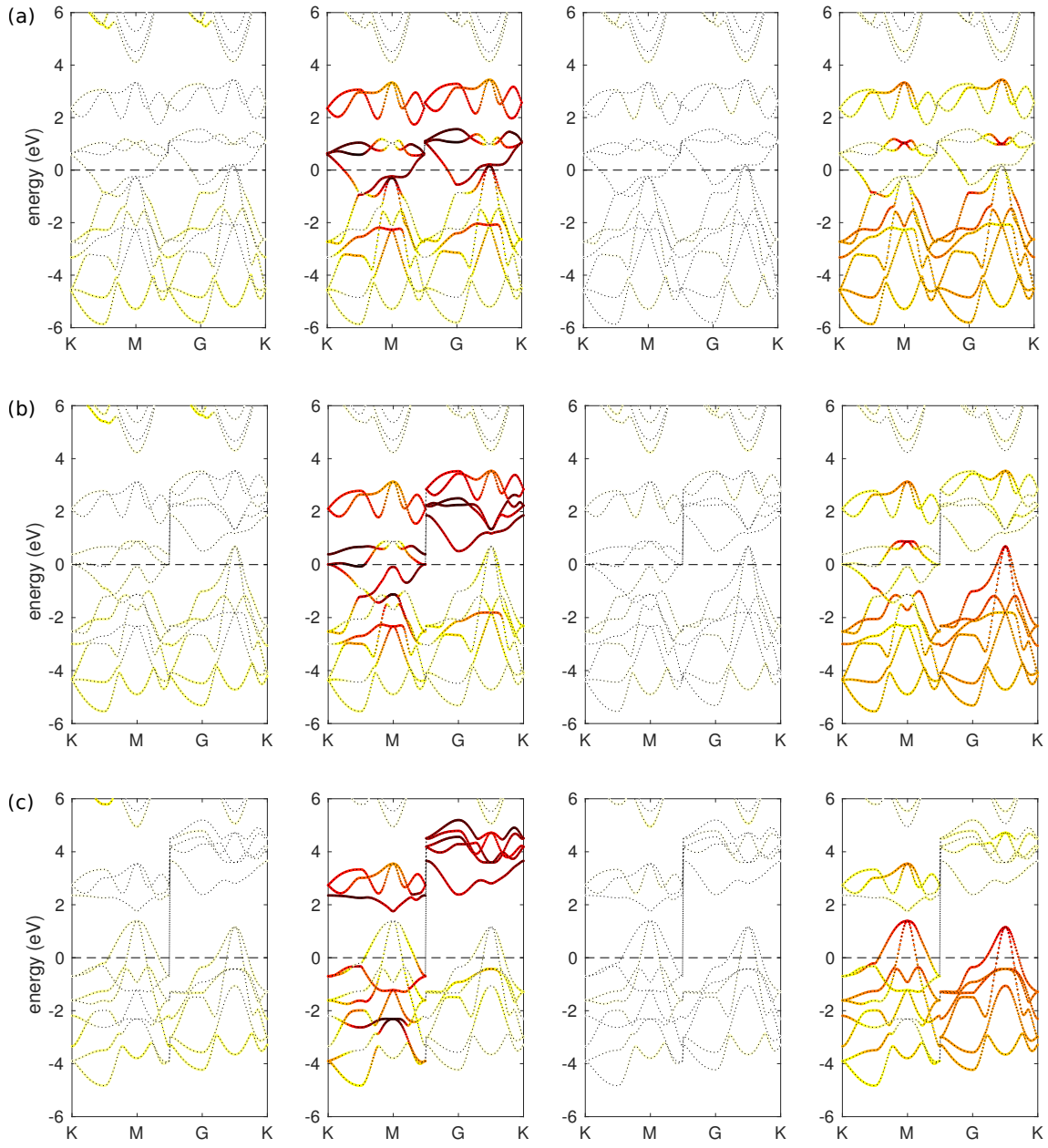

Supplementary Figure 5. Band structure of monolayer T-VSe_2 calculated using (a) revB86b, (b) revB86b+U(2), and (c) revB86b+U(5), projected on V-sp, V-d, Se-s, and Se-p, respectively in the four columns. Half of the k-points are spin up and half are spin down. Energy zero is at Fermi-level.

The preferential stacking has Se of VSe_2 on top of hexagon hole of $NbSe_2$ and V on top of Nb (CaB). The binding is clearly weakest when the Se of VSe_2 is on top of Se of $NbSe_2$. The binding energies clearly correlate with the interlayer distance. Strongest binding energy

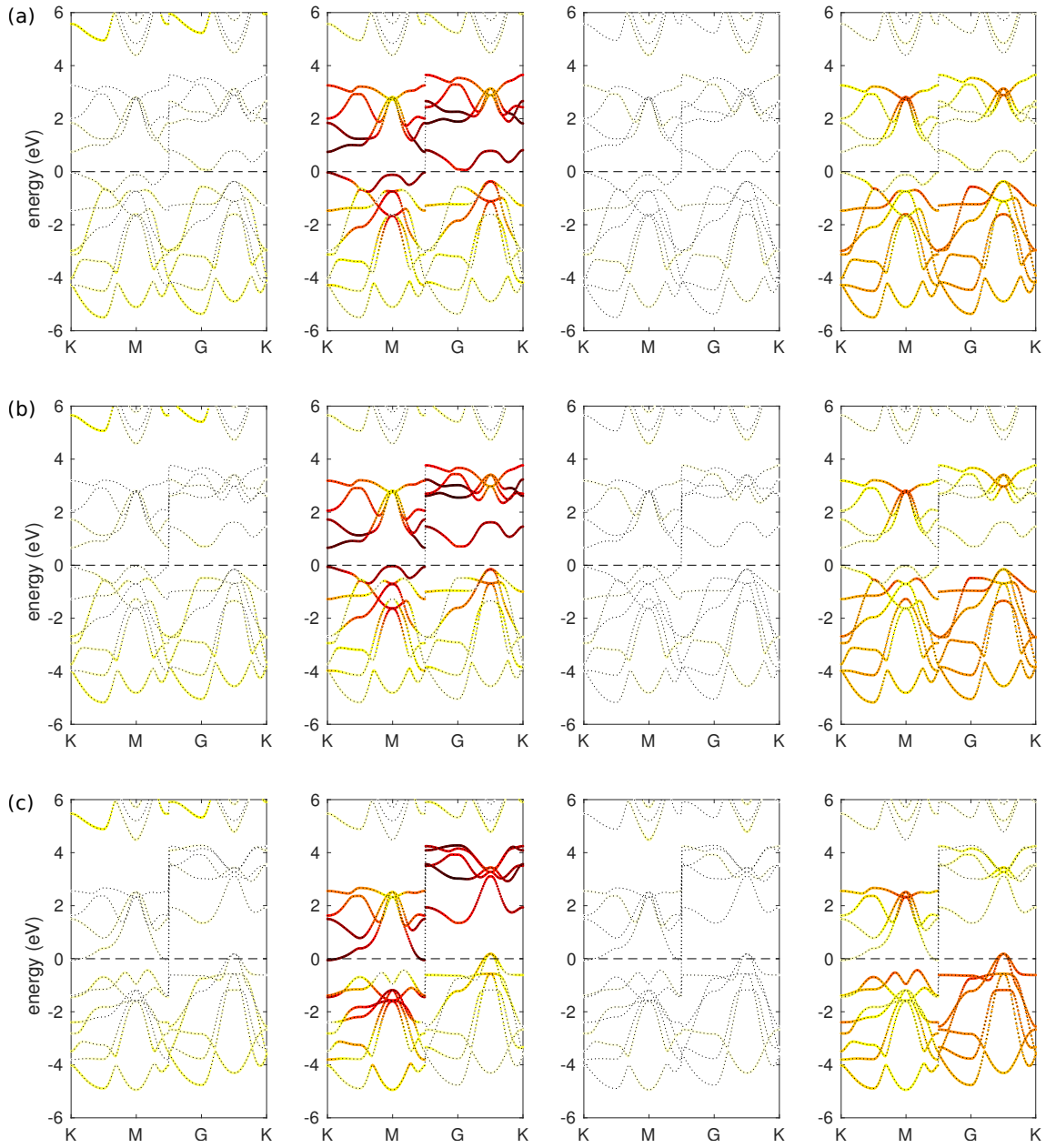

Supplementary Figure 6. Band structure of monolayer H-VSe_2 calculated using (a) revB86b, (b) revB86b+U(2), and (c) revB86b+U(5), projected on V-sp, V-d, Se-s, and Se-p, respectively in the four columns. Half of the k-points are spin up and half are spin down. Energy zero is at Fermi-level.

corresponds to closest distance.

The charge transfer and dipole over the heterostructure seem similar in all cases, and generally quite small, e.g., 0.01 e from VSe_2 to $NbSe_2$ in CaB case (about 10^{13} cm^{-2}). Such

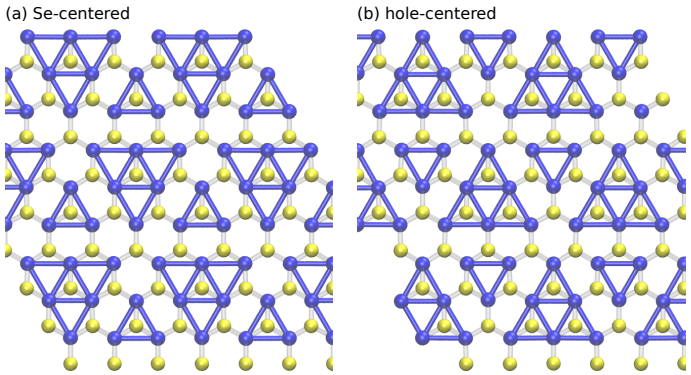

Supplementary Figure 7. Atomic structure of $NbSe_2$ in the charge-density wave (CDW) phase.

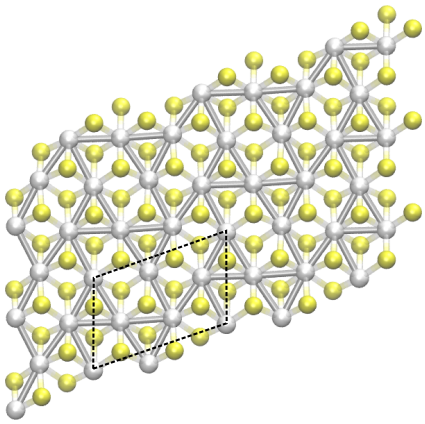

Supplementary Figure 8. Atomic structure of VSe_2 in the charge-density wave (CDW) phase. Parallelogram depicts the CDW unit cell.

charge transfer should be insufficient to destroy CDW ordering of the $NbSe_2$ under VSe_2.

Supplementary Figure 9 shows the BaB/CaB heterostructure band structure projected to $NbSe_2$ and VSe_2 layers, calculated using revB86b+U(2). There are no dramatic changes due to stacking. By comparing to the orbital projections in Figs. 4 and 5 it can be seen that the largest changes occur whenever the bands have strong Se-p contribution, which can feel the other layer.

Densities of states (DOS) of the heterostructure and the isolated monolayers are shown in Supplementary Figure 10.

Simulated STM images: STM images of the $NbSe_2$ and VSe_2 are shown in Supplementary Figure 11. The constant height image is recorded at 3 Å from the topmost Se atom

Supplementary Table 3. Properties of the H-$NbSe_2$/T-VSe_2 heterostructures: interlayer binding energy E_b, total magnetization per unit cell M, distance between the Nb and V layers h_{Nb-V}, and the dipole over the heterostructure p. The first set is without $+U$ correction and the second with $U = 2$ eV.

	AbC	AcB	BaC	BcA	CaB	CbA
E_b (eV)	-0.249	-0.272	-0.175	-0.144	-0.287	-0.222
M (μ_B)	0.96	0.92	0.95	0.0	0.95	0.0
E_b (eV)	-0.239	-0.259	-0.166	-0.168	-0.269	-0.250
h_{Nb-V} (Å)	6.34	6.23	6.76	6.76	6.16	6.24
p (meVÅ)	14.0	14.2	14.5	14.1	14.4	14.6
M (μ_B)	1.19	1.14	1.15	1.16	1.14	1.20

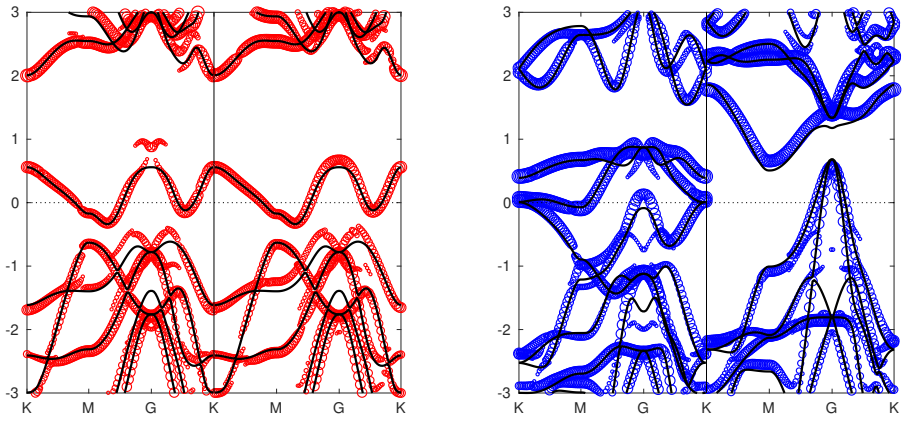

Supplementary Figure 9. Band structure projected to $NbSe_2$ (left, red) and VSe_2 (right, blue) layers from the BaB/CaB stacked heterostructure. The band structure from pristine monolayers are shown with black lines. Fermi-level is set to zero in all band structures. Left/right half is spin-up/down.

and the constant current image at different small isosurface values, which is the same for different biases, but different in different materials. For the non-CDW phases they all look similar, with protrusions at Se atoms. For the CDW-$NbSe_2$, the experimental images shown in the main text have close match with the simulated images in the HC-phase.

The simulated STM image for CDW-VSe_2 is in good agreement with the experimental

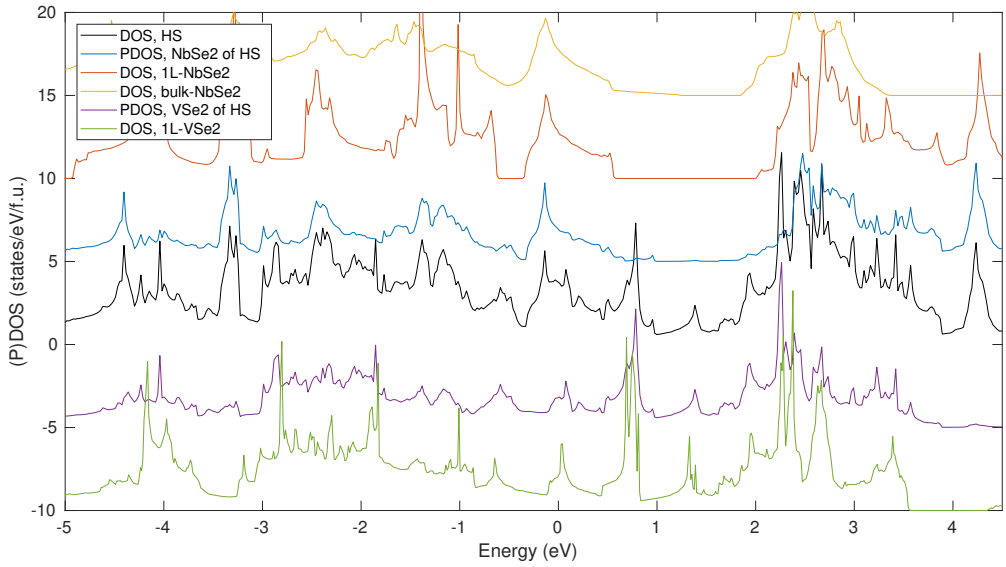

Supplementary Figure 10. Density of states (DOS) of the heterostructure is shown in the middle. Above/below are the contributions to it from $NbSe_2$/VSe_2 layers, and above/below those are the DOSes of pristine $NbSe_2$/VSe_2 monolayers for comparison. The spin-up and -down channels are summed up. Fermi-level is set to zero.

images reported in [8], but not observed in our experiments.

Simulated STS: STS is simulated within Tersoff-Hamann approach using LDOS as

$$I(E) = \sum_{E<E_i<E+\delta E} \int \rho_i(x, y, z = z_0) \mathrm{d}x\mathrm{d}y \tag{1}$$

where $\rho_i = |\Psi_i|^2$ is the partial charge density of ith Kohn-Sham orbital, z_0 determines the distance above the surface, and δE sets the energy resolution; here 20 meV.

LDA and revB86b in the NM phase show a very prominent peak at Fermi-level that is in poor agreement with experiments. The same is true for the LDA result in FM phase due to very small magnetic moment. The simulated spectra for the CDW phase seems consistent with the dip at the Fermi-level and the step-like structure at positive energies seen in the experimental spectra, although (i) in the calculations the dip is about 0.15 eV above Fermi-level and (ii) the dip appears to be present already in the $NbSe_2$ spectrum. Point (i) would contradict with the expected hole-doping from the calculated work functions. Although point (ii) suggests $NbSe_2$ origin for the dip, the dip becomes more pronounced in the bilayer spectrum. These features could be a signature of the CDW phase in the bilayer region,

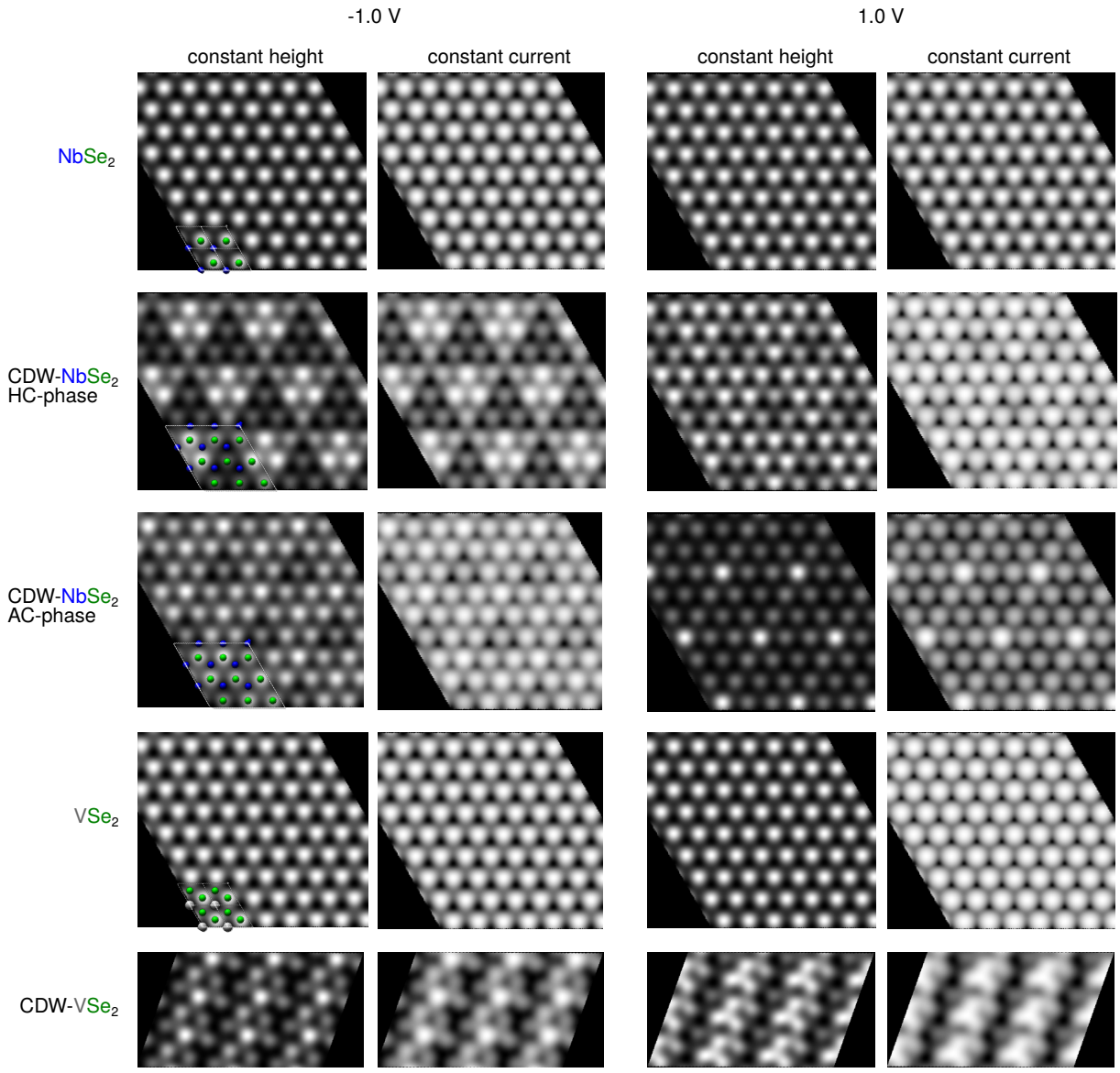

Supplementary Figure 11. Simulated scanning tunneling microscopy (STM) images of (a) pristine no-charge-density wave (CDW) $NbSe_2$, (b) CDW-$NbSe_2$ hexagon-centered phase, (c) CDW-$NbSe_2$ anion-centered phase, (d) no-CDW VSe_2, and (e) CDW-VSe_2. The atomic structures are overlaid.

which makes sense as bulk VSe_2 is known to exhibit CDW and also the bilayer regions are very small and thus strongly affected by the edges. On the other hand, these features are fairly weak in the monolayer spectrum and there is also an additional peak at 1.5 eV and the change in the peak shape at around -0.5 eV. These changes are consistent with the change between the revB86b calculated CDW and FM phases. The peak around 1.5 eV becomes more pronounced and the peak at -0.05 eV in CDW phase moves down to -0.3 eV in the

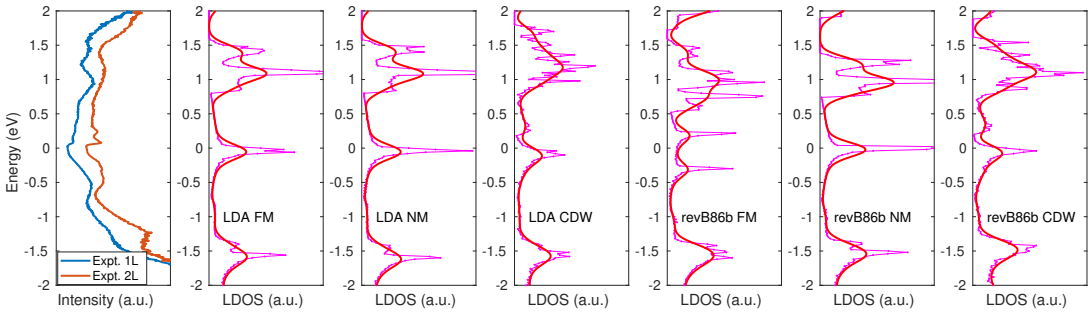

Supplementary Figure 12. Comparison of simulated scanning tunneling spectroscopy (STS) evaluated using two different exchange-correlation (XC) functionals and in three different phases: ferromagnetic (FM), nonmagnetic (NM), and charge density wave (CDW). Magenta curves show the bare spectra and red curves have been smoothed to allow for more direct comparison with the experimental one.

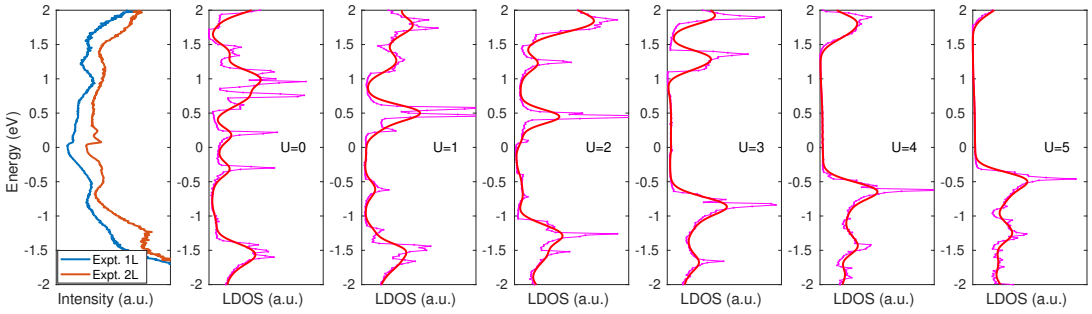

Supplementary Figure 13. The evolution of simulated scanning tunneling spectroscopy (STS) with increasing $+U$ parameter (revB86b functional) and comparison to the experimental spectrum.

FM phase.

The corresponding results for H-VSe_2 are shown in Supplementary Figure 14. The simulated spectra without $+U$ is in reasonably good agreement with the experimental spectra, but not with $+U$.

Increasing the value of the U-parameter to 1–2 eV the lower energy features appear to be in good agreement with experiment, but there is an extraneous strong peak at about $E_F + 0.5$ eV. At $U \geq 3$ eV, the agreement becomes rather poor.

The band structure, density of states, simulated STS, and experimental STS calculated using revB86b+U(2) are shown in Supplementary Figure 15 and can be compared to the

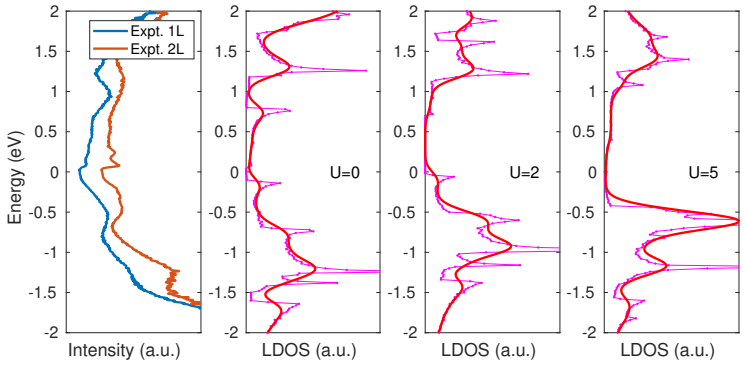

Supplementary Figure 14. The evolution of simulated scanning tunneling spectroscopy (STS) of H-VSe_2 with increasing $+U$ parameter (revB86b functional) and comparison to the experimental spectrum.

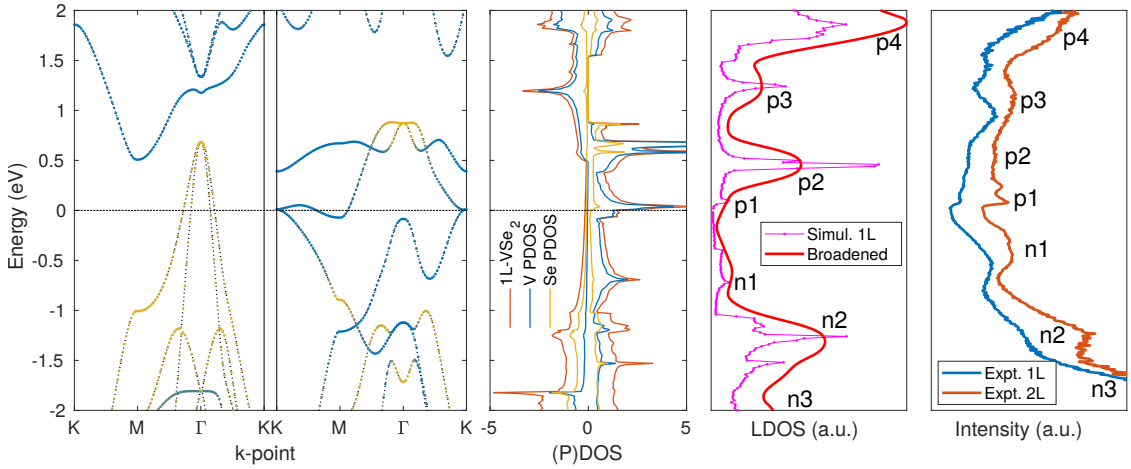

Supplementary Figure 15. Band structure, density of states, simulated scanning tunneling spectroscopy (STS), and experimental STS calculated using revB86b+U(2). The peaks are denoted as in the main text.

revB86b calculated results in Fig. 3 in the main paper.

Finally, the band structure and density of states of the bilayer T-VSe_2 (adopting AA stacking as in bulk VSe_2) are shown in Supplementary Figure 16. The two bands are generally split by less than 0.2 eV. The density of states shows splitting of the main peaks which agrees rather well with the features seen in the experimental STS: the splitting of the peaks above and below Fermi-level.

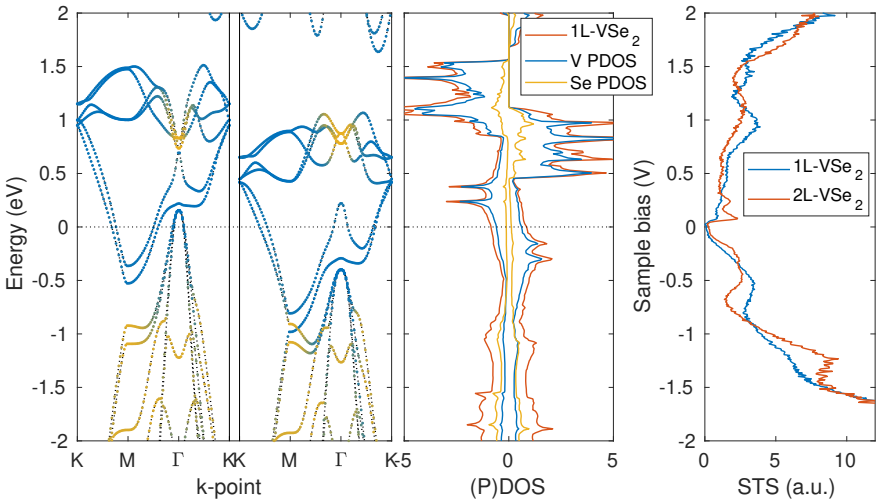

Supplementary Figure 16. Band structure and density of states of bilayer T-VSe_2 calculated using revB86b compared with the experimental scanning tunneling spectroscopy (STS) data.

SUPPLEMENTARY NOTE 3: RAW DATA BEFORE AND AFTER REMOVING MONOLAYER VSe_2

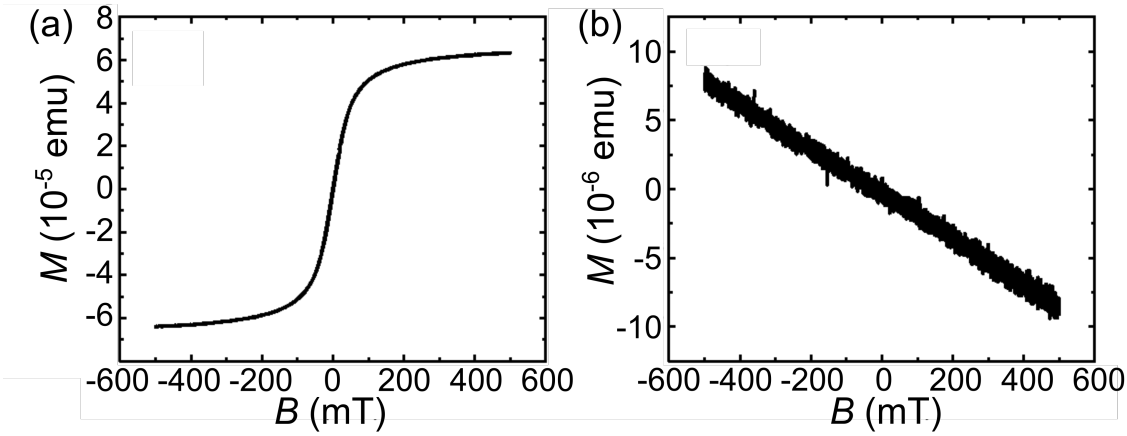

Supplementary Figure 17. Raw vibrating sample magnetometry (VSM) data before and after removing monolayer VSe_2 by cleaving the sample. (a) The raw $M-H$ curve of ML VSe_2 on $NbSe_2$ taken at 300 K using VSM. (b) The raw $M-H$ curve of $NbSe_2$ after cleaving the same sample to remove the monolayer VSe_2 taken at 300 K using VSM.

SUPPLEMENTARY NOTE 4: FIT OF BRILLOUIN FUNCTION TO MAGNETIZATION DATA

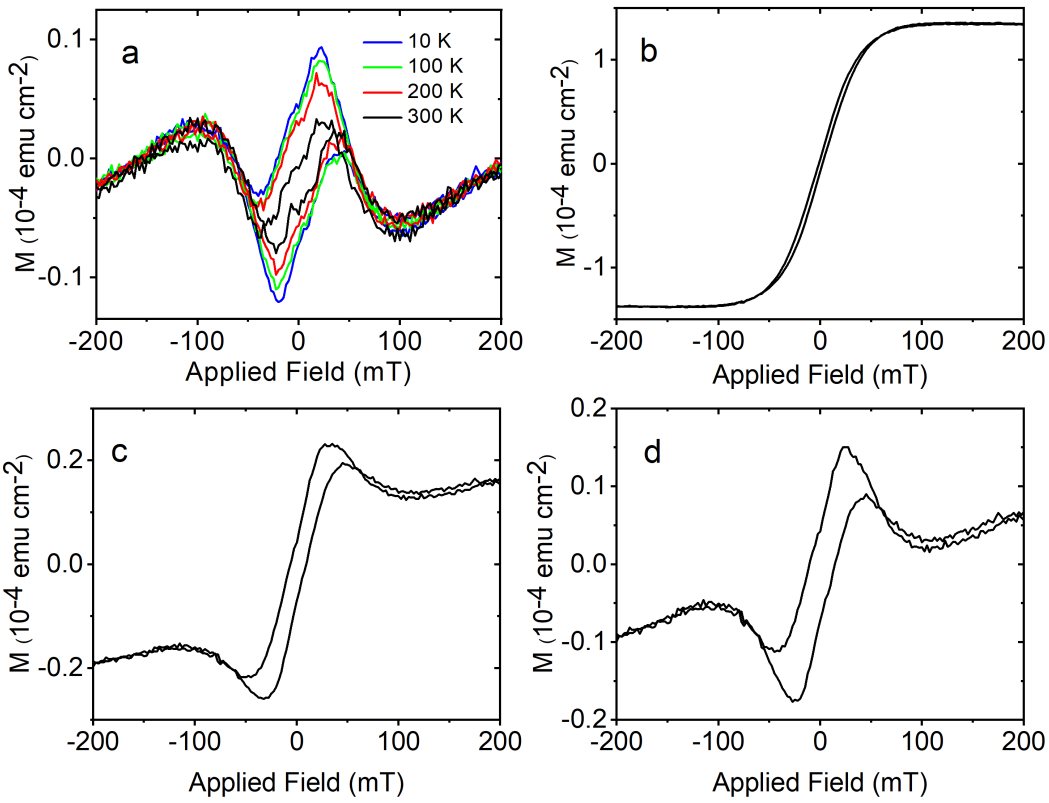

Supplementary Figure 18. (a) The result of the magnetization data minus the Brillouin function and linear background, where the fit was over all the magnetic field range excluding the ferromagnetic term for 10 K, 100 K, 200 K and 300 K measurements. (b) Result of the 10 K magnetization data minus the Brillouin fit and linear background where the fitting included the ferromagnetic part of the function but the fit is limited to fields > 100 mT and < -100 mT. (c) As b but with a 10 mT cut-off field. (d) As b and c but fitting the whole magnetic field range.

It has been shown in a $MnSe_2$/GaSe system by O'Hara *et al.* [11] that magnetization measurements on monolayer samples can be complicated by a paramagnetic background signal. In their case, they attributed this to Mn atoms incorporated in the substrate during MBE growth. We fit the model proposed by O'Hara *et al.* to our data assuming the presence of a background paramagnetic signal. The model consists of a Brillouin paramagnetic term

along with a linear background and a ferromagnetic part:

$$m(H) = A_{\mathrm{lin}} \cdot H + A_{\mathrm{para}} \cdot \frac{2J+1}{2J} \coth\left(\frac{2J+1}{2J} \cdot \frac{g^* \mu_{\mathrm{B}} J H}{k_{\mathrm{B}} T}\right) - \frac{1}{2J} \coth\left(\frac{1}{2J} \cdot \frac{g^* \mu_{\mathrm{B}} J H}{k_{\mathrm{B}} T}\right) + \mathrm{sign}(H) \cdot m_{\mathrm{sat}} \quad (2)$$

where m is the magnetization, H is the magnetic field, A_{lin} parameterizes a linear background, A_{para} is the scaling factor for the Brillouin term, J is the total angular momentum quantum number, which we take to be 3/2 in this case, g^* is the effective g-factor, μ_{B} is the Bohr magneton, k_{B} is the Boltzmann constant, T is the temperature and m_{sat} is the saturation magnetization. In the main paper the equation above excluding the ferromagnetic part ($\mathrm{sign}(H) \cdot m_{\mathrm{sat}}$) is used to fit the whole magnetic field range for the 10 K data in Fig. 4a. The difference between the fit and data is shown in the inset to Fig. 4b and this is reproduced in Supplementary Figure 18a, along with the same plot for the other temperatures measured. Different results can be obtained by including the ferromagnetic part of equation and by fitting to a different magnetic field range, as suggested in O'Hara *et al.* This leads to various different results for the result of the data minus the Brillouin fit (so nominally the ferromagnetic signal) as shown in Supplementary Figure 18b-d. Figure 18b fits the data only outside there magnetic field range where hysteresis occurs, and leads to the largest apparent ferromagnetic signal. By including more of the magnetic field data the plots in Supplementary Figure 18c,d are obtained. The persistence of a clear hysteretic part of the fitting indicates that the sample likely gives some ferromagnetic response, consistent with what is inferred from local scanning probe measurements, but that it is not possible to clearly identify its magnitude due to the much larger paramagnetic signal.

SUPPLEMENTARY NOTE 5: TEMPERATURE DEPENDENCE OF $H - M$ LOOP

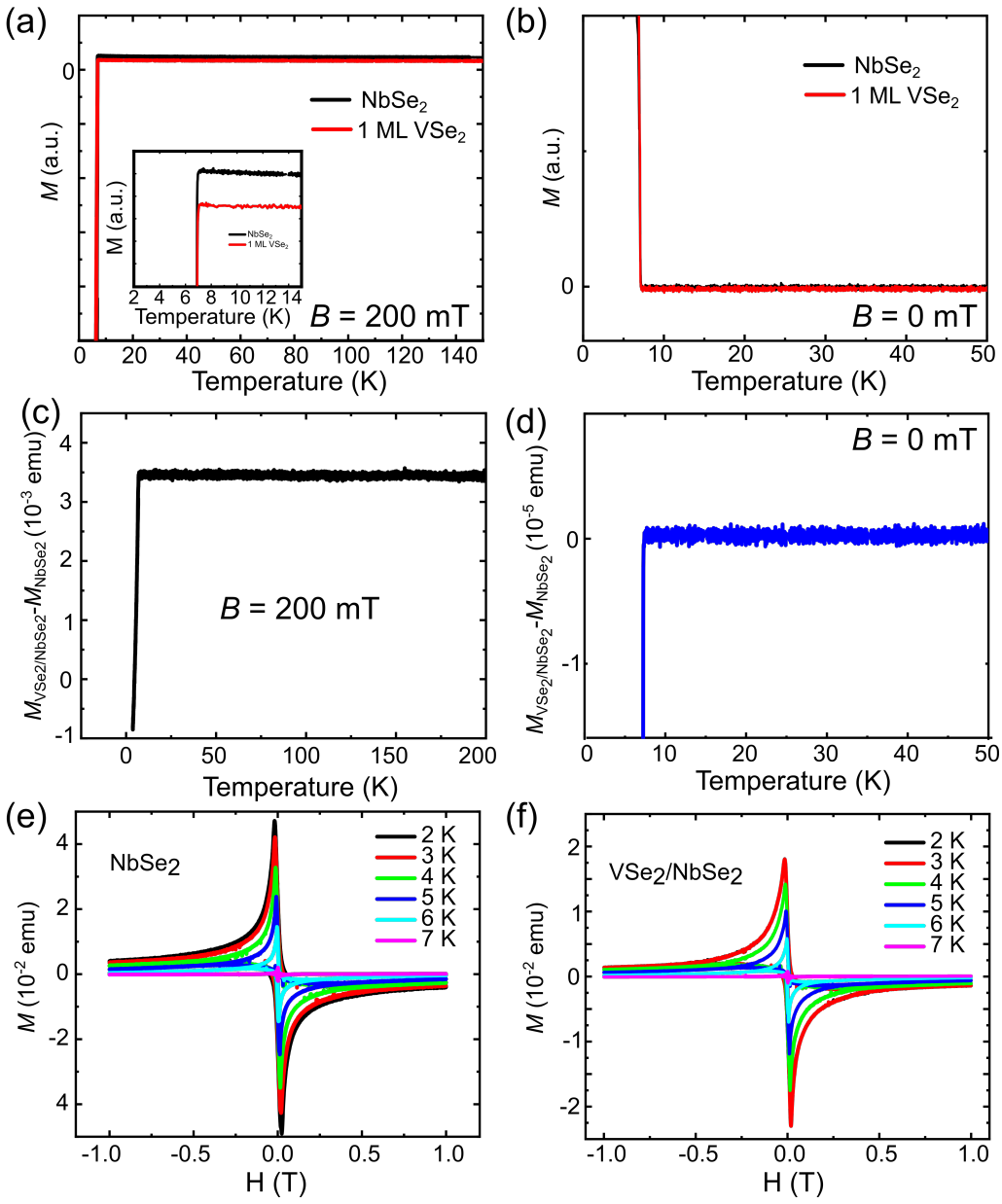

Supplementary Figure 19. Superconductivity in the VSe_2/ $NbSe_2$ hybrids. (a,b) Temperature-dependent field cooling (FC) (magnetic field of 200 mT) and zero-feld cooling (ZFC) magnetization measurements for VSe_2 on $NbSe_2$. (c,d) Background subtracted FC and ZFC (panel c) and zero-field cooling (panel d). (e,f) The temperature dependent $M(H)$ hysteresis loop for the $NbSe_2$ single crystal and VSe_2/ $NbSe_2$ hybrids, respectively.

SUPPLEMENTARY NOTE 6: EFFECT OF THE SUBSTRATE TEMPERATURE

The quality of the sample (e.g. the sharpness of the VSe_2 edges) can be improved by growing the sample at a high substrates temperatures. Supplementary Figure 20a shows STM characterization of sub-monolayer VSe_2 films on $NbSe_2$ substrate grown at $T = 600$ K. The edge of the island is much sharper compare with low growth temperature, which is grown at $T = 540$ K (Supplementary Figure 20c). However, at high temperature growth, the metal atom starts to intercalate $NbSe_2$ and as a result of that the $NbSe_2$ substrate loses the long-range charge density wave order as shown in an atomic resolution STM image (Supplementary Figure 20b). In our experiment, we have optimized the substrate temperature ($T = 540 - 570$ K) to insure that the long-range charge density wave order is preserved (Supplementary Figure 20d). The metal intercalation not only affects the charge density wave order but also the superconducting gap. Supplementary Figure 20e shows the $\mathrm{d}I/\mathrm{d}V$ spectra measured on $NbSe_2$ surface with and without a metal intercalation.

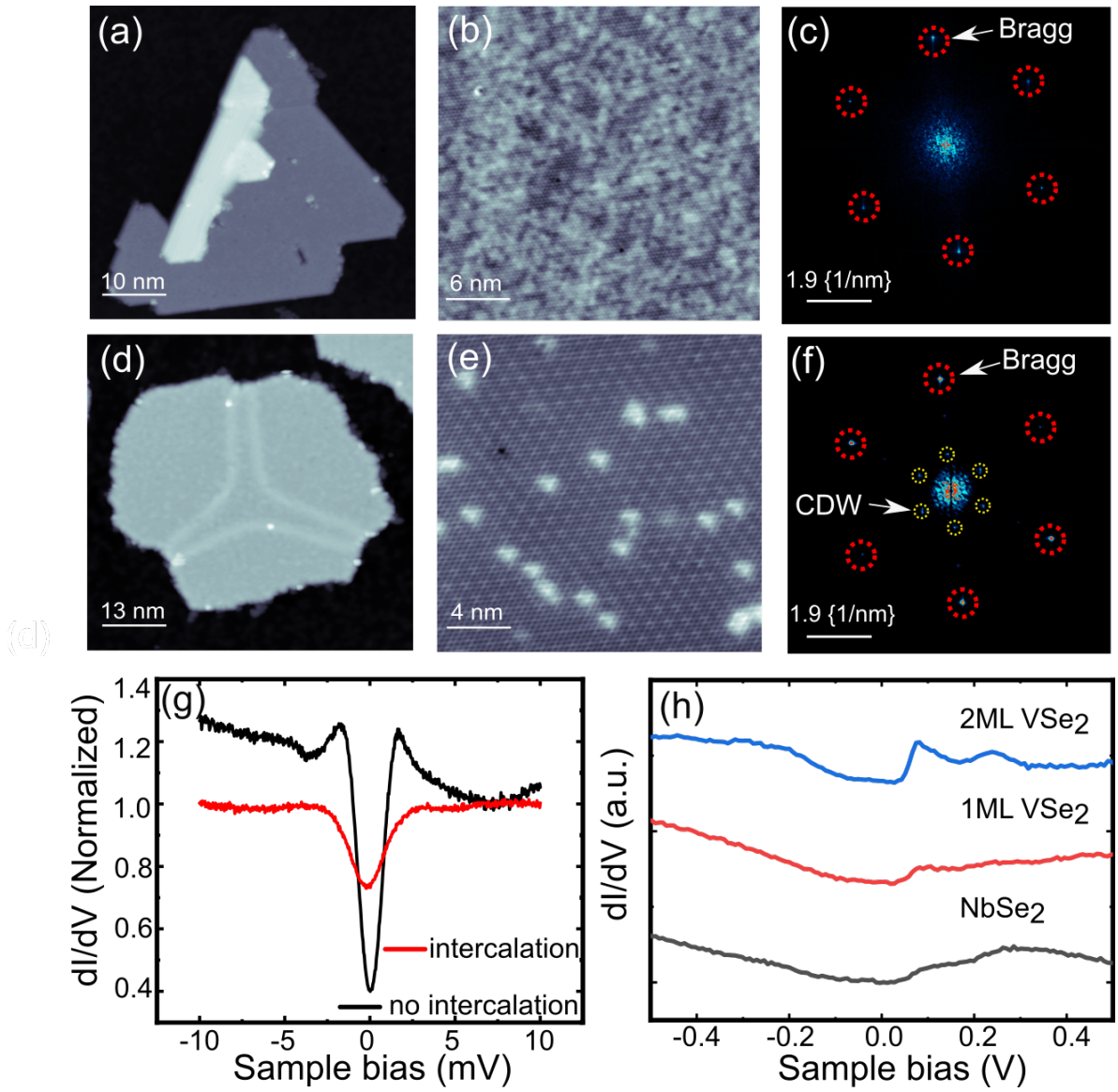

Supplementary Figure 20. VSe_2 growth on $NbSe_2$ at different substrate temperatures. (a) Scanning tunneling microscopy (STM) topographic image (1 V, 10 pA) of VSe_2 on $NbSe_2$ grown at $T = 600$ K. (b) Atomic resolution STM image (10 mV, 1 nA) of $NbSe_2$ surface showing an absence of charge density wave super-structures due to the intercalation. (c) Fast Fourier transform (FFT) of the atomic resolution image in panel (b). (d) STM topographic image (1 V, 10 pA) of VSe_2 on $NbSe_2$ grown at $T = 540$ K. (e) Atomic resolution STM image (10 mV, 1 nA) of $NbSe_2$ surface showing a hexagonal lattic with charge density wave super-structures. (f) FFT of the atomically resolved image shown in panel(e). (f) dI/dV spectra measured on the $NbSe_2$ substrate with and without intercalation, respectively. (h) Short-range spectra on the $NbSe_2$ and VSe_2 mono- and bilayer showing the absence of a strong charge-density wave (CDW) gap on VSe_2.

SUPPLEMENTARY NOTE 7: FITTING THE SUPERCONDUCTING GAP

While $NbSe_2$ is better described as a two-gap (or anisotropic gap) superconductor, the $\mathrm{d}I/\mathrm{d}V$ spectra at not too low temperatures can be adequately fit with the standard BCS expression with the density-of-states (D_s) given by [12]

$$D_\mathrm{s}(\epsilon) = \begin{cases} 0 & \epsilon < \Delta \\ \epsilon/(\epsilon^2 - \Delta^2)^{1/2} & \epsilon > \Delta \end{cases} \tag{3}$$

The thermal broadening at temperature T is taken into account in the calculation of the $\mathrm{d}I/\mathrm{d}V$ signal

$$\frac{\mathrm{d}I}{\mathrm{d}V}(V_\mathrm{b}) \propto \int_\infty^\infty D_\mathrm{s}(\epsilon) \frac{\exp((V_\mathrm{b}+\epsilon)/k_\mathrm{B}T)}{(1+\exp((V_\mathrm{b}+\epsilon)/k_\mathrm{B}T))^2} \mathrm{d}\epsilon \tag{4}$$

where V_b is the applied bias voltage. This expression was then used to fit the experimental $\mathrm{d}I/\mathrm{d}V$ spectra with Δ as a fitting parameter.

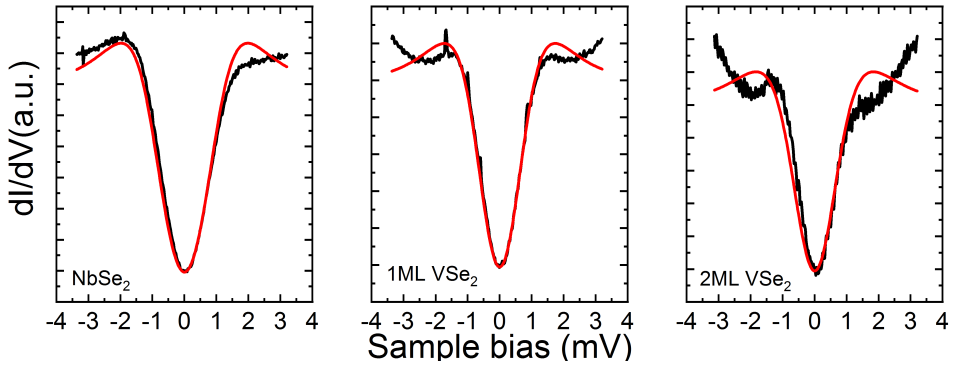

Supplementary Figure 21. Dependence of the superconducting gap on the number of VSe_2 layers. Experimental $\mathrm{d}I\mathrm{d}V$ data (black lines) and the corresponding fits using the BCS density of states (Eq. 3).

SUPPLEMENTARY NOTE 8: EVOLUTION OF THE EDGE STATE OF MONOLAYER VSe_2

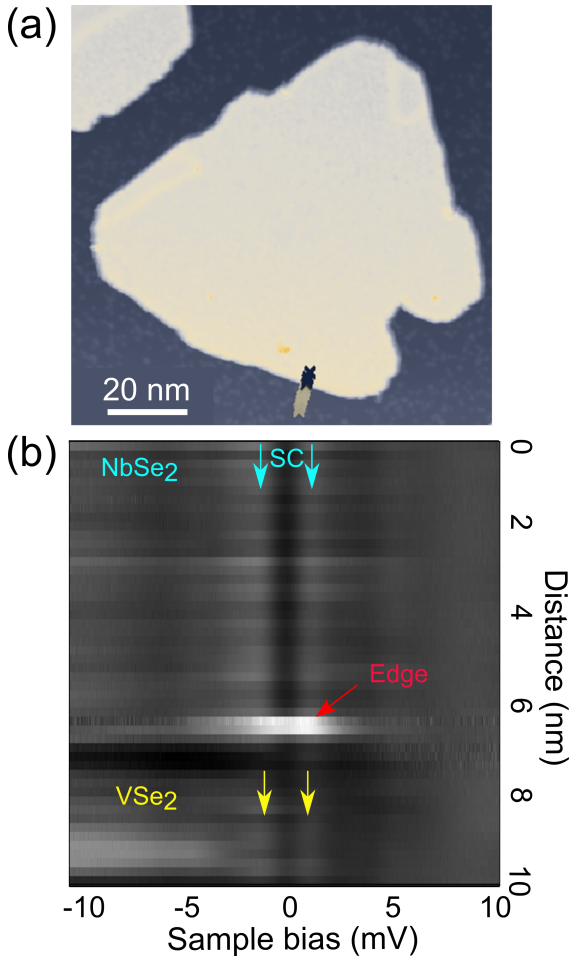

Supplementary Figure 22. Localized edge mode of VSe_2 on $NbSe_2$. (a) Scanning tunneling microscopy (STM) topographic image (1 V, 10 pA) of VSe_2 on $NbSe_2$ (b) A line spectra taken along the edge of island where its width can be a couple of times larger than the superconducting gap width.

Supplementary Figure 22b shows a linecut profiles of $\mathrm{d}I/\mathrm{d}V$ spectra along the line in Supplementary Figure 22a, which cross the edge of the VSe_2. As the tip approaches the island edge, the superconducting coherence peaks (arrows in the Supplementary Figure 22b) in the $\mathrm{d}I/\mathrm{d}V$ spectra are suppressed and new electronic states emerge inside the gap as shown by the highlighted red arrow in Supplementary Figure 22b. The superconducting coherence peaks further reduce on top of the VSe_2.

SUPPLEMENTARY NOTE 9: SAMPLE QUALITY AT DIFFERENT PREPARATION CONDITIONS

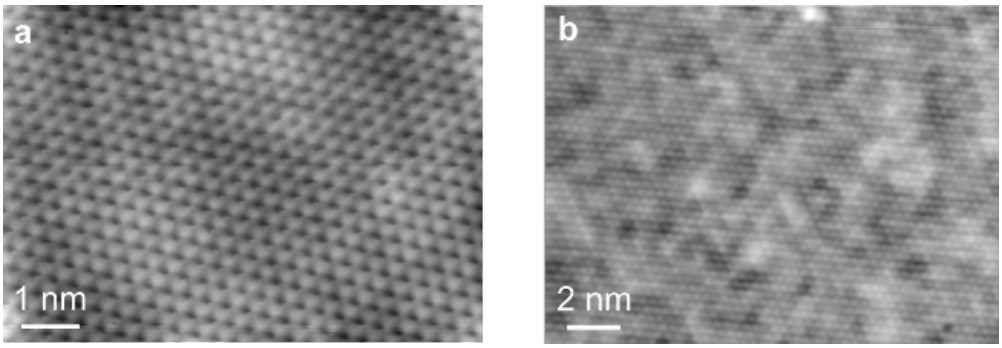

Supplementary Figure 23. Atomically resolved scanning tunneling microscopy (STM) images of the VSe_2 lattice. (a) Sample corresponding to the usual preparation conditions. (b) VSe_2 growth carried out at a higher temperature resulting in significant intercalation of vanadium.

Supplementary Figure 23 shows atomically resolved images on two completely different sample preparations carried out at different substrate temperatures of 270 °C and of ca. 300 °C, respectively. Supplementary Figure 23a corresponds to the usual sample preparation conditions (the slightly visible superstructure matches the CDW of the underlying $NbSe_2$ substrate). Supplementary Figure 23b shows an image from a sample preparation carried out at a higher temperature, where we get significant vanadium intercalation (visible as the background contrast variation). In both cases, the VSe_2 lattice constant is 3.5 ± 0.1 Å and we do not observe a CDW.

SUPPLEMENTARY REFERENCES

[1] Kresse, G. & Hafner, J. Ab initio molecular dynamics for liquid metals. *Phys. Rev. B* **47**, 558–561 (1993).

[2] Kresse, G. & Furthmüller, J. Efficiency of ab-initio total energy calculations for metals and semiconductors using a plane-wave basis set. *Comp. Mat. Sci.* **6**, 15–50 (1996).

[3] Blöchl, P. E. Projector augmented-wave method. *Phys. Rev. B* **50**, 17953–17979 (1994).

[4] Fumega, A. O. & Pardo, V. Absence of ferromagnetism in VSe_2 caused by its charge density wave phase, arXiv:1804.07102 .

[5] Perdew, J. P., Burke, K. & Ernzerhof, M. Generalized gradient approximation made simple. *Phys. Rev. Lett.* **77**, 3865 (1996).

[6] Grimme, S. Semiempirical GGA-type density functional constructed with a long-range dispersion correction. *J. Comput. Chem.* **27**, 1787 (2006).

[7] Hamada, I. Van der Waals density functional made accurate. *Phys. Rev. B* **89**, 121103 (2014).

[8] Coelho, P. M. *et al.* Charge density wave state suppresses ferromagnetic ordering in VSe_2 monolayers. *J. Phys. Chem. C* **123**, 14089–14096 (2019).

[9] Malliakas, C. D. & Kanatzidis, M. G. Nb-Nb interactions define the charge density wave structure of $2H$-$NbSe_2$. *J. Am. Chem. Soc.* **135**, 1719–1722 (2013).

[10] Gye, G., Oh, E. & Yeom, H. W. Topological landscape of competing charge density waves in $2H-NbSe_2$. *Phys. Rev. Lett.* **122**, 016403 (2019).

[11] O'Hara, D. J., Zhu, T. & Kawakami, R. Importance of paramagnetic background subtraction for determining the magnetic moment in epitaxially grown ultrathin van der Waals magnets. *IEEE Magn. Lett.* **9**, 1405805 (2018).

[12] Hudson, E. W. *Investigating High-Tc Superconductivity on the Atomic Scale by Scanning Tunneling Microscopy* (Ph.D. Thesis, University of California, Berkeley, 1999).